communications physics

A Nature Portfolio journal

Article

https://doi.org/10.1038/s42005-026-02634-3

Optimising germanium hole spin qubits with a room-temperature magnet

Check for updates

Cécile X. Yu [1,3], Barnaby van Straaten [1,3], Alexander S. Ivlev [1], Valentin John [1], Damien R. Crielaard [1], Stefan D. Oosterhout [2], Lucas E. A. Stehouwer [1], Francesco Borsoi [1], Giordano Scappucci [1] & Menno Veldhorst [1]

Germanium spin qubits offer high-fidelity control via strong spin-orbit interaction, but their magnetic field sensitivity typically requires bulky superconducting vector magnets that limit scalability. This study investigates replacing these with an external permanent magnet located outside the cryostat to reclaim internal sample space. By operating in a hybrid mode (internal and external magnets), we fine-tuned the field to an in-plane orientation, achieving a dephasing time $T_2^* = 13\,\mu s$ and single-qubit Clifford gate fidelities exceeding 99.9%. Remarkably, we demonstrate qubit operation even with the internal superconducting magnet deactivated. In this regime, we observed extended coherence times of $T_2^* = 31\,\mu s$ and $T_2^{H} = 266\,\mu s$, on a natural Germanium heterostructure. These results demonstrate that room-temperature magnets allow for high qubit performance. This approach facilitates scaling by freeing cryogenic space for essential control circuitry and wiring, paving the way for large-scale quantum processors.

Spin qubits in semiconductor quantum dots are an attractive platform for quantum computing, as they offer long coherence times, allow for high-fidelity quantum gates, and have high compatibility with industrial semiconductor fabrication[1]. Germanium has emerged as a promising material for hosting hole-based spin qubits, offering strong spin-orbit interaction and all-electrical control[2–5]. Despite these advantages, achieving precise control over the qubit properties requires accurate alignment of the external magnetic field to the substrate plane to optimise coherence and fidelity due to the strong *g*-tensor anisotropy[6–9].

Even if the *g*-tensor plane is aligned with the sample crystallographic axes, achieving sub-degree accuracy in magnetic field alignment is challenging due to factors such as sample mounting variability and the differential thermal contraction of materials within the cryostat. While vector magnets can compensate for these misalignments to minimise hyperfine-induced dephasing and enhance the efficiency of electric dipole spin resonance (EDSR) operations[6,10], their implementation requires considerable space and thermal load within the cryostat, and limits the available sample space[11].

This work explores an alternative approach using a movable permanent magnet outside the dilution refrigerator to fine-tune the magnetic field at the qubit location in addition to the uniaxial superconducting magnet in the cryostat. This internal magnet provides a primary magnetic field of a few tens of millitesla, chosen to be small enough that any misalignment can be effectively corrected using the external magnet.

To characterise the feasibility of this approach, we perform EDSR drive on the qubit to evaluate its resonance frequency as a function of the uniaxial superconducting magnetic field strength, as well as the position of the external magnet relative to the sample. This study is further extended by characterising the qubit performance through Ramsey and Hahn echo experiments, along with single-qubit gate randomised benchmarking (RB) and gate set tomography. Our findings demonstrate that a qubit fine-tuned by an external magnet can achieve high-quality qubit control, with fidelities exceeding 99.9%. We then switch off the uniaxial superconducting magnet to demonstrate that qubit operation is possible with the field produced by the permanent magnet only. We characterise the qubit properties under this field, finding long coherence times.

Results and discussion

Experimental set-up

In this experiment, we use a standard cryogen-free dilution refrigerator equipped with a uniaxial superconducting magnet. To fine-tune the magnetic field, we move an NdFeB N45 block magnet of dimensions $110.6 \times 89 \times 19.5$ mm, in three dimensions beneath the fridge (see Fig. 1a). The motion of the external magnet is accomplished by suspending a Cartesian gantry system from the vacuum can of the dilution refrigerator, with motion along the *x*, *y*, and *z* axes controlled remotely by linear actuators and an Arduino board. A complete description of the system is provided in Supplementary Note 1.

[1]QuTech and Kavli Institute of Nanoscience, Delft University of Technology, Delft, The Netherlands. [2]QuTech and Netherlands Organisation for Applied Scientific Research, Delft, The Netherlands. [3]These authors contributed equally: Cécile X. Yu, Barnaby van Straaten. e-mail: M.Veldhorst@tudelft.nl

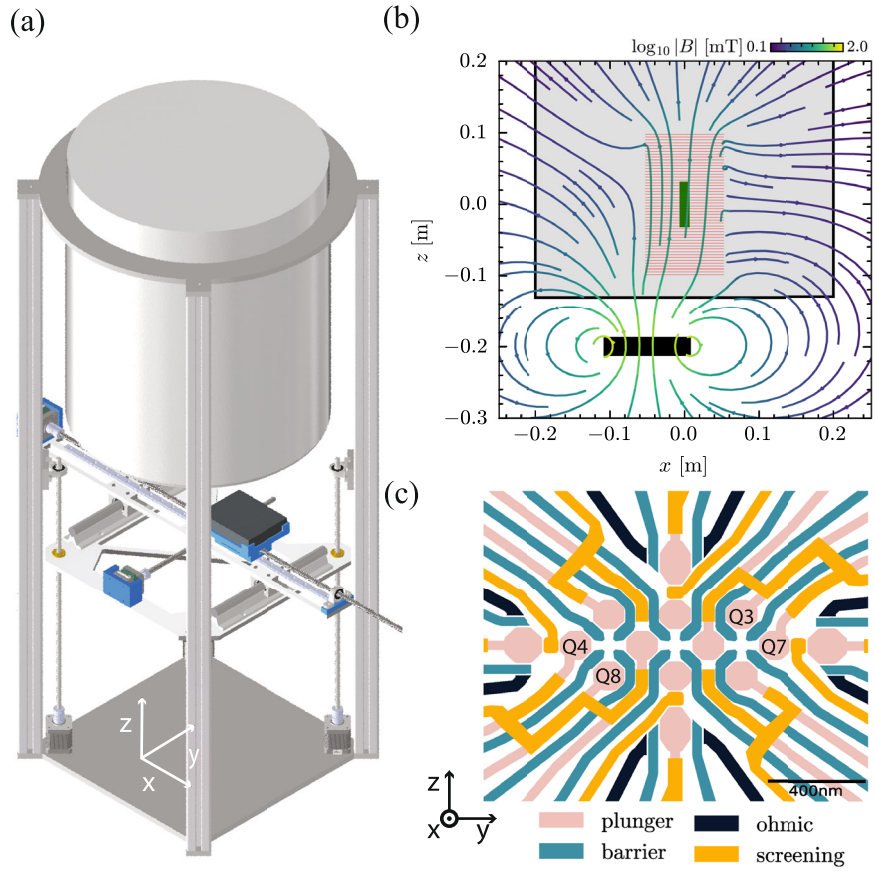

Fig. 1 | Experimental set-up. a Diagram showing the XYZ stage used to position the permanent magnet (grey block). The stage is attached to the vacuum can of the fridge. **b** Diagram showing a simulation of the magnetic field lines produced by the superconducting solenoid magnet (red) and the permanent magnet (black). The sample board is shown in green, mounted in the centre of the solenoid magnet. The colourbar represents the strength of the magnetic field. **c** Device layout indicating the qubits investigated in the experiments. The scale bar corresponds to 400 nm.

For our coordinate system, we take the z axis as parallel to the vertical axis of the dilution refrigerator. If the sample were mounted perfectly, fields applied in this direction correspond to the [110] crystallographic direction and therefore are in-plane. In previous work on this device[12], we estimate there is a 2–3 degree misalignment, meaning that the magnetic field of the internal superconducting solenoid has a small out-of-plane component. We define the x axis close to parallel to the heterostructures [001] growth direction; therefore, fields applied in this direction are out of plane. The permanent magnet was oriented with its magnetisation axis along the z axis, so that at $x, y = 0$, its field is parallel to that of the solenoid, see Fig. 1b for a Magpylib simulation of the field lines[13]. By moving the magnet in the x direction, we expect to be able to compensate and cancel out the orthogonal field component, provided the external magnetic field is sufficiently strong.

We perform our qubit experiments on a 10-quantum dot device on a Ge/SiGe heterostructure as detailed in ref. 9,12, and investigate the effect of the magnetic field. We focus on qubits Q8 and Q3, which are initialised and read out using ancilla qubits Q4 and Q7, respectively, see Fig. 1c. The coordinate system is defined relative to the sample, meaning that $(x, y, z) = (0, 0, 0)$ corresponds to the sample. We will refer to the magnetic field applied by the superconducting uniaxial solenoid inside the fridge as $\mathbf{B}_{\text{in}}$, and $\mathbf{B}_{\text{ext}}$ as the magnetic field generated by the external magnet.

Qubit frequency tunability

We begin by assessing the effect of the external magnet on the total magnetic field sensed by the spin qubit. The total field sensed by the qubit is $\mathbf{B}_T = \mathbf{B}_{\text{ext}} + \mathbf{B}_{\text{in}}$, which gives rise to a qubit Larmor frequency of $hf_L = \mu_B|g\mathbf{B}_T|$, where g is the germanium hole-spin g-tensor[6]. Relative to gyromagnetic axes of the spins, we anticipate this g-tensor to take the form $g = \text{diag}(g_x, g_y, g_z)$ with significant anisotropy such that $g_z \gg g_x, g_y$. We expect the axis corresponding to g_z to be aligned to within a few degrees with the crystallographic [001] axis and therefore also to within a few degrees of the x axis. We will label this axis $\widehat{\mathbf{g}}_z$.

To probe the effect of $\mathbf{B}_{\text{ext}}$, we perform EDSR on qubit Q8 while varying the external magnet position along the x axis from 0 to −250 mm, with the magnet held at $(y, z) = (0, -200)$ mm. For each position, we map the qubit Larmor frequency at different amplitudes of the internal field $\mathbf{B}_{\text{in}}$. As the external magnet is displaced, both B_x^{ext} and B_z^{ext} vary, leading to a change in the orientation of the total field $\mathbf{B}_T$ relative to $\widehat{\mathbf{g}}_z$. Because of the large anisotropy in g, even small components of $\mathbf{B}_T$ parallel to $\widehat{\mathbf{g}}_z$ strongly affect the enhanced g-factor and hence the Larmor frequency.

At low $|\mathbf{B}_{\text{in}}|$ (see Fig. 2a, b), the resonance frequency exhibits both a minimum and a local maximum as a function of magnet position. The minimum corresponds to the point where B_z^{ext} cancels the out-of-plane contribution parallel to $\widehat{\mathbf{g}}_z$ of $\mathbf{B}_{\text{in}}$ and thereby minimising the effective g-factor. Moving the magnet further off-axis, B_z^{ext} begins to overcompensate the internal field while the magnitude of $\mathbf{B}_{\text{ext}}$ at the qubit decreases with distance. This competition produces a local maximum in the Larmor frequency before it falls off again.

At larger $|\mathbf{B}_{\text{in}}|$ (see Fig. 2c, d), the external field is no longer strong enough to fully cancel the out-of-plane component of $\mathbf{B}_{\text{in}}$, and the resonance frequency evolves smoothly with a parabolic dependence on the magnet position. Finally, we note that in the low-field regime of Fig. 2a, b, the qubit initialisation and readout fidelity decrease as the total field rotates from out-of-plane to in-plane. We attribute this to reduced initialisation of the $|\uparrow\downarrow\rangle$ state: in-plane fields enhance the quantisation-axis mismatch between the two qubits, which increases the probability of preparing the $|T_-\rangle = |\downarrow\downarrow\rangle$ state[14].

Now we set $|\mathbf{B}_{\text{in}}| = 25$ mT and fully characterise the tunability of the Larmor frequency in the xz- and xy-planes as shown in Fig. 3. The Larmor frequency, f_L, varies from 50 MHz to 150 MHz, with the x axis playing the dominant role by determining the out-of-plane component of the total magnetic field, and thus causing the strongest tunability on the qubit frequency. In the xz-plane, the qubit resonance frequency exhibits a minimum corresponding to the optimal field orientation where the external magnet

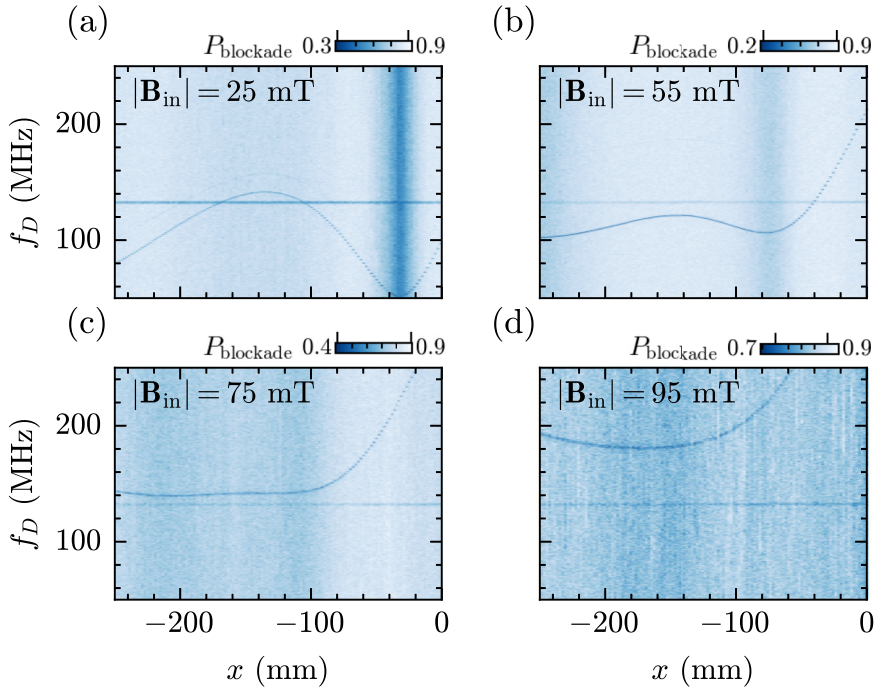

Fig. 2 | Effect of the internal magnetic field magnitude. Microwave spectroscopy of qubit frequency versus magnet x-position ($y = 0$, $z = -200$ mm). Internal magnetic field magnitudes for **a**–**d** are 25, 55, 75, 95 mT, respectively. P_{blockade} defines the probability of the even spin state being blockaded, and f_D is the microwave drive tone frequency. The resonance ~130 MHz corresponds to the resonance frequency of the readout resonator. The colour bars represent the probability of Pauli spin blockade upon measurement.

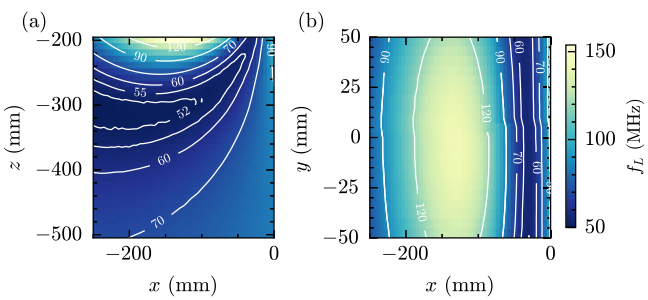

Fig. 3 | Experimentally measured Larmor frequencies of the qubit as a function of magnet position at $|\mathbf{B}_{\text{in}}| = 25$ mT. a Larmor frequency in the xz-plane of the permanent magnet at $y = 0$ mm. **b** Larmor frequency in the xy-plane of the permanent magnet at $z = -200$ mm. The colourbar represents the measured Larmor frequency for each magnet position. The contour lines are defined by connecting the corresponding experimental data points.

compensates the internal magnetic field, resulting in a fully in-plane configuration. In contrast, in the xy-plane, variations in magnet position primarily tune the in-plane magnetic field orientation.

Qubit coherence times

We now focus on the qubit performance at the magnetic field sweet spot to enhance the qubit dephasing times. We fix the z-position to −200 mm and the y-position to zero, while the x-position is varied around the point corresponding to the minimum Larmor frequency. At this position, the magnetic field is expected to be aligned within the plane of the sample, where dephasing noise is minimised due to the hyperfine interactions with nuclear spins being minimal[6,15]. Thus, to enhance the qubit dephasing times, the magnetic field has to be aligned perpendicular to the growth direction, where the anisotropic hyperfine interaction between heavy hole states and nuclear spins is expected to be negligible[15].

We measure the coherence times of Q8 by means of Ramsey and Hahn echo experiments to probe the impact of field tuning on spin coherence, as shown in Fig. 4. We find that when the Larmor frequency reaches its minimum value, T_2^* and T_2^{H} are simultaneously maximised, indicating an in-plane magnetic field orientation. By orienting the magnetic field fully in-plane at the hyperfine noise sweet spot, the dephasing time of the qubit reaches $T_2^* = 13.41 \pm 0.53$ µs while the echo time $T_2^{\text{H}} = 88.77 \pm 9.99$ µs. This is comparable with coherence times measured at the magnetic field sweet spot in a vector magnet[6]. Qubit Q3 also exhibits the same trend as a function of the external magnet position along the x direction, see Supplementary Note 2. For comparison, without the external magnet, the Ramsey and Hahn echo experiments on Q8 (see Supplementary Note 3) indicate coherence times of $T_2^* = 1.70 \pm 0.12$ µs and $T_2^{\text{H}} = 4.23 \pm 0.11$ µs, respectively, revealing a hyperfine noise-limited regime[12]. In Supplementary Note 4, we also show the Rabi drive efficiency of Q8 as a function of the magnet x-position. It reveals a peak in drive efficiency that coincides with the maximum coherence time, indicating that, for this qubit, an in-plane magnetic field is beneficial for both long coherence times and fast driving[6,7].

We furthermore evaluate the single-qubit gate fidelity using both RB and gate set tomography (GST). We perform RB using the Clifford set detailed in Supplementary Note 4, giving us an average Clifford fidelity of $F_{\text{C}} = 99.936 \pm 0.005\%$. Detailed methods and results for the GST are provided in Supplementary Note 5. By dividing the average gate fidelity by the number of native gates per Clifford operation, we obtain a single-qubit gate fidelity of 99.980 ± 0.002%, comparable to the highest reported values for qubits and measured using vector magnets[6,16]. GST, which is more sensitive to systematic errors, reports average fidelities of 99.95 ± 0.02% for the $X90$ gate and 99.88 ± 0.02% for the $Y90$ gate (see Supplementary Note 5). The lower fidelities reported by GST are expected to come from dynamical decoupling effects present in the RB sequence[17]. Supplementary Note 7 displays additional qubit coherence and fidelity data as a function of the magnet position with the device in a different electrostatic configuration.

Zero internal field operation

A key challenge in scaling towards large-scale quantum processors is represented by the limited space available at the base temperature in a cryostat [18]. By removing the superconducting magnet inside the cryostat, the available sample space can be increased substantially, allowing for more control lines and improved prospects of scalability.

Here, we simulate this scenario by switching off the internal magnetic field, such that the qubit only senses the magnetic field of the permanent magnet. In this configuration, we measure the Larmor frequency as a function of the external magnet's position along the x axis. By tuning the magnet position to the point where the qubit Larmor frequency reaches its

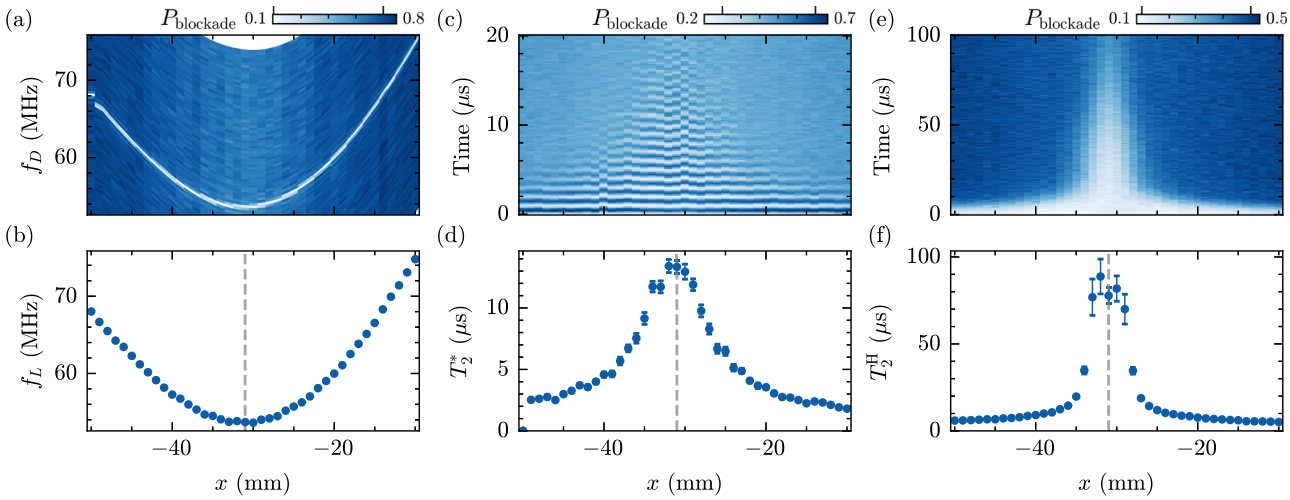

Fig. 4 | Qubit coherence times at the magnetic field's sweet spot. a, **b** Larmor frequency f_L as a function of the x-position of the permanent magnet extracted from the microwave spectroscopy. The colour bars represent the probability of Pauli spin blockade upon measurement. **c**, **d** Dephasing times T_2^* as a function of the magnet position in x measured with a Ramsey sequence. **e**, **f** T_2^{H} measured with a Hahn echo sequence. The dashed grey lines indicate the optimal field spot at the minimum of the Larmor frequency, where the magnetic field points in-plane. The error bars represent the precision of the fit.

Fig. 5 | Zero internal field qubit Larmor, Rabi, Ramsey, and Hahn echo. Measured with the external magnet at (x, y, z) = (−7, 0, −200) mm. **a** Qubit Larmor resonance, along with the fit to extract the qubit Larmor frequency. **b** Qubit Rabi oscillations along with the fit to extract the qubit Rabi frequency. **c** Ramsey oscillations along with the fit to extract T_2^*, with an integration time of 30 mins. **d** Hahn echo with the qubit initialised in both the up and down states, along with the fit to extract T_2^{H}.

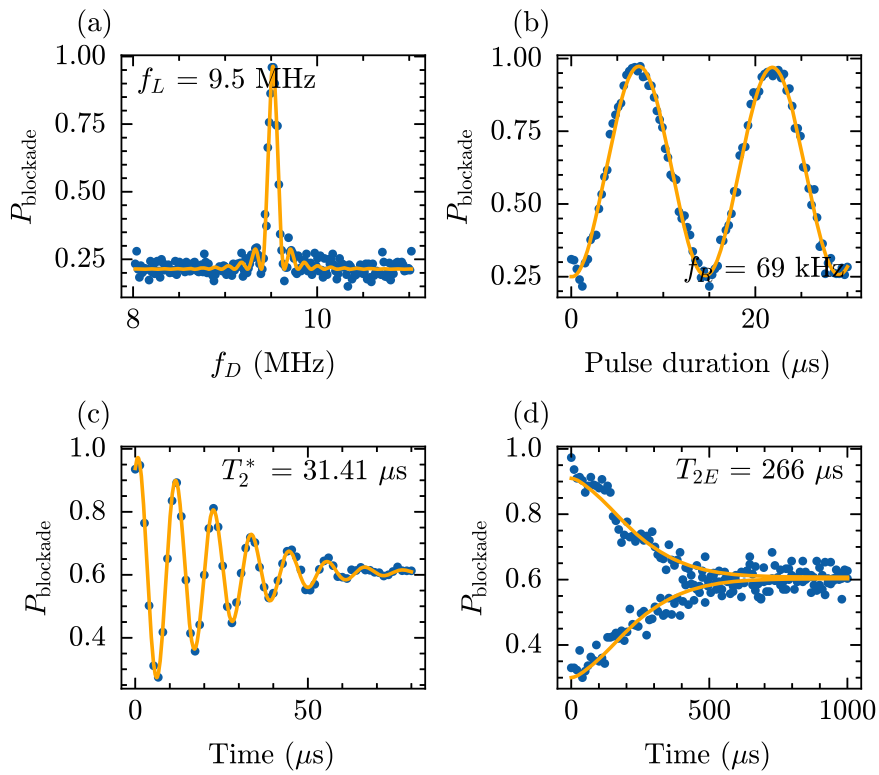

minimum, ~9.5 MHz, we identify the optimal operating field (see Fig. 5a, b). This process was slightly complicated by a small hysteretic effect in the magnet position, discussed in supplementary note 8. At this working point, we re-optimise the initialisation and readout pulse sequence using an optimiser based on ref. 19. We then observe long coherence times of $T_2^* = 31.4\,\mu\text{s}$ and $T_2^{\text{H}} = 266.0\,\mu\text{s}$ for hole-spin qubits in germanium (see Fig. 5c, d). We attribute these long coherence times to the suppression of charge noise at low magnetic fields, as well as to the reduced hyperfine interactions achieved by aligning the magnetic field in the plane.

However, operating at low magnetic fields also reduces the achievable Rabi frequency. Under these conditions, we obtain a Rabi frequency of $f_R = 52$ kHz using a drive amplitude of $A = 8.4$ mV at the sample. Consistent with the slow Rabi frequency, we measure single-qubit Clifford gate fidelities of 99.7% using EDSR, confirmed through RB, see Supplementary Note 9.

By contrast, hopping-based gates are expected to operate at rates orders of magnitude faster than EDSR, with characteristic frequencies that reach a substantial fraction of the qubit Larmor frequency[4]. Incorporating such hopping gates could therefore dramatically accelerate qubit control in the low-field regime, enabling fast, high-fidelity spin manipulation without requiring large magnetic fields. Should EDSR be required, higher magnetic fields at the device level up to 1 T could be achieved using a block magnet

that can be placed inside the cryostat near the qubit chip[20,21]. This can be combined with a room-temperature permanent magnet to fine-tune the magnetic field orientation for optimal qubit operations.

Conclusion

Superconducting magnets inside dilution refrigerators require considerable space and can introduce current noise or ground loops into the qubit system. We demonstrate that a room-temperature permanent magnet offers an effective alternative to fine-tune the magnetic field experienced by germanium spin qubits. Our versatile room-temperature magnet set-up enables in-plane magnetic field alignment, allowing natural germanium devices to operate in regimes less affected by hyperfine noise, thereby enhancing qubit coherence and gate fidelity. Even qubits hosted in isotopically purified materials[22,23] will need to be tuned to optimal operating conditions[9], which can similarly be done with the external magnet approach presented here. The cryostat space may then be used to integrate control wiring and cryo electronics for the construction of large-scale quantum hardware.

Methods

The spin qubit device is fabricated on a Ge/SiGe heterostructure as detailed in ref. 12. The device is cooled down in a Bluefors LD400 dilution fridge equipped with an uniaxial solenoid magnet up to 3 T in the z axis at a base temperature of 10 mK. The uniaxial magnet is operated in the driven mode except when it is turned off. The NdFeB N45 block magnet is commercially available under article ID Q-111-89-20-E, its dimensions are $110.6 \times 89 \times 19.5$ mm, and it has an adhesive force of 200 kg. Its magnetic field strength is probed using 3D magnetic Hall sensors integrated on a printed circuit board (ref. TLE493D-P3XX-MS2GO).

In the experiments, we initialise the qubit by pulsing from the (0,2) singlet state to the centre of the (1,1) state adiabatically to prepare a $|\uparrow,\downarrow\rangle$ state. We then perform qubit manipulation via EDSR before reading out the spin state using Pauli spin blockade readout. The DC voltages are set to the device via an in-house built SPI rack (https://qtwork.tudelft.nl/~mtiggelman/spi-rack/chassis.html), and AC controls are generated using a Keysight M3202A arbitrary waveform generator.

Data availability

The data and analysis code supporting the findings of this study are openly available in the 4TU.ResearchData repository under https://doi.org/10.4121/eb6053c1-e70c-401c-914e-576e612869a5.

Received: 14 July 2025; Accepted: 9 April 2026;
Published online: 29 April 2026

References

1. Burkard, G., Ladd, T. D., Pan, A., Nichol, J. M. & Petta, J. R. Semiconductor spin qubits. *Rev. Mod. Phys.* **95**, 025003 (2023).
2. Watzinger, H. et al. A germanium hole spin qubit. *Nat. Commun.* **9**, 1–6 (2018).
3. Hendrickx, N. W. et al. A four-qubit germanium quantum processor. *Nature* **591**, 580–585 (2021).
4. Wang, C. A. et al. Operating semiconductor quantum processors with hopping spins. *Science* **385**, 447–452 (2024).
5. Scappucci, G. et al. The germanium quantum information route. *Nat. Rev. Mater.* **6**, 926–943 (2020).
6. Hendrickx, N. W. et al. Sweet-spot operation of a germanium hole spin qubit with highly anisotropic noise sensitivity. *Nat. Mater.* **23**, 920–927 (2024).
7. Mauro, L., Rodríguez-Mena, E. A., Bassi, M., Schmitt, V. & Niquet, Y. M. Geometry of the dephasing sweet spots of spin-orbit qubits. *Phys. Rev. B* **109**, 155406 (2024).
8. Saez-Mollejo, J. et al. Exchange anisotropies in microwave-driven singlet-triplet qubits. *Nat. Commun.* **16**, 1–9 (2025).
9. John, V. et al. Robust and localised control of a 10-spin qubit array in germanium. *Nat. Commun*. **16**, 1432 (2025).
10. Bassi, M. et al. Optimal operation of hole spin qubits. *Nat. Phys.* **22**, 75–80 (2025).
11. Da Prato, G., Yu, Y., Bode, R. & Gröblacher, S. Step-by-step design guide of a cryogenic three-axis vector magnet. *Rev. Sci. Instrum.* **96**, 063001 https://doi.org/10.1063/5.0270187 (2025).
12. Stehouwer, L. E. A. et al. Exploiting strained epitaxial germanium for scaling low-noise spin qubits at the micrometre scale. *Nat. Mater.* **24**, 1906–1912 (2025).
13. Ortner, M. & Bandeira, L. G. C. Magpylib: a free python package for magnetic field computation. *SoftwareX* **11**, 100466 (2020).
14. Jirovec, D. et al. Dynamics of hole singlet-triplet qubits with large g -factor differences. *Phys. Rev. Lett.* **128**, 126803 (2022).
15. Fischer, J., Coish, W. A., Bulaev, D. V. & Loss, D. Spin decoherence of a heavy hole coupled to nuclear spins in a quantum dot. *Phys. Rev. B* **78**, 155329 (2008).
16. Lawrie, W. I. et al. Simultaneous single-qubit driving of semiconductor spin qubits at the fault-tolerant threshold. *Nat. Commun.* **14**, 1–7 (2023).
17. Dehollain, J. P. et al. Optimization of a solid-state electron spin qubit using gate set tomography. *N. J. Phys.* **18**, 103018 (2016).
18. Mohseni, M. et al. How to build a quantum supercomputer: scaling from hundreds to millions of qubits. Preprint at https://arxiv.org/abs/2411.10406 (2024).
19. Katiraee-Far, S. R. et al. Unified evolutionary optimization for high-fidelity spin qubit operations. Preprint at https://arxiv.org/abs/2503.12256 (2025).
20. Adambukulam, C. et al. An ultra-stable 1.5 T permanent magnet assembly for qubit experiments at cryogenic temperatures. *Rev. Sci. Instrum.* **92**, 085106 (2021).
21. Rooney, J. et al. Gate modulation of the hole singlet-triplet qubit frequency in germanium. *npj Quantum Inf.* **11**, 1–7 (2025).
22. Moutanabbir, O. et al. Nuclear spin-depleted, isotopically enriched 70Ge/28Si70Ge quantum wells. *Adv. Mater.* **36**, 2308965 (2024).
23. Chekhovich, E. A. et al. Nuclear spin effects in semiconductor quantum dots. *Nat. Mater.* **12**, 494–504 (2013).

Acknowledgements

We are grateful to Jason Mensingh for providing the external magnet, Nico Alberts and Tim Hiep for the fine precision mechanics. This research was supported by the European Union through the Horizon 2020 research and innovation programme under the Grant Agreement No. 951852 (QLSI) and the Horizon Europe Framework Programme under grant agreement No. 101069515 (IGNITE). F.B. and M.V. acknowledge support from the NWO through the National Growth Fund programme Quantum Delta NL (grant NGF.1582.22.001). This research was sponsored in part by the Army Research Office (ARO) under Award No. W911NF-23-1-0110 and by The Netherlands Ministry of Defence under Awards No.QuBits R23/009. The views, conclusions, and recommendations contained in this document are those of the authors and are not necessarily endorsed nor should they be interpreted as representing the official policies, either expressed or implied, of the Army Research Office (ARO) or the U.S. Government, or the Netherlands Ministry of Defence. The U.S. Government and the Netherlands Ministry of Defence are authorised to reproduce and distribute reprints for Government purposes, notwithstanding any copyright notation herein.

Author contributions

C.X.Y. and B.v.S. conducted the experiments and performed the analysis with support from V.J and D.R.C. A.S.I. conceived and constructed the experimental set-up. V.J and F.B designed the device. S.D.O. fabricated the device, L.E.A.S. and G.S. supplied the heterostructures. C.X.Y., B.v.S., and M.V. wrote the manuscript with input from all authors. M.V. supervised the project.

Competing interests

M.V. and G.S. are founding advisors of Groove Quantum BV and declare equity interests. The remaining authors declare no competing interests.

Additional information

Supplementary information The online version contains supplementary material available at https://doi.org/10.1038/s42005-026-02634-3.

Correspondence and requests for materials should be addressed to Menno Veldhorst.

Peer review information *Communications Physics* thanks John Nichol and the other, anonymous, reviewer for their contribution to the peer review of this work. A peer review file is available.

Reprints and permissions information is available at http://www.nature.com/reprints

Publisher's note Springer Nature remains neutral with regard to jurisdictional claims in published maps and institutional affiliations.

Open Access This article is licensed under a Creative Commons Attribution 4.0 International License, which permits use, sharing, adaptation, distribution and reproduction in any medium or format, as long as you give appropriate credit to the original author(s) and the source, provide a link to the Creative Commons licence, and indicate if changes were made. The images or other third party material in this article are included in the article's Creative Commons licence, unless indicated otherwise in a credit line to the material. If material is not included in the article's Creative Commons licence and your intended use is not permitted by statutory regulation or exceeds the permitted use, you will need to obtain permission directly from the copyright holder. To view a copy of this licence, visit http://creativecommons.org/licenses/by/4.0/.

© The Author(s) 2026